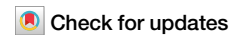


<https://doi.org/10.1038/s43246-024-00542-z>

# Crack mitigation in additively manufactured AlCrFe<sub>2</sub>Ni<sub>2</sub> high-entropy alloys through engineering phase transformation pathway



Shahryar Mooraj<sup>1,7</sup>, Xizhen Dong<sup>2,7</sup>, Shengbiao Zhang<sup>1,7</sup>, Yanming Zhang<sup>3</sup>, Jie Ren<sup>1</sup>, Shuai Guan<sup>1</sup>, Chenyang Li<sup>4</sup>, Rameshwari Naorem<sup>5</sup>, Nicolas Argibay<sup>6</sup>, Wei Chen<sup>4</sup>, Wentao Yan<sup>3</sup>, Dierk Raabe<sup>2</sup>, Zhongji Sun<sup>2,6</sup> ✉ & Wen Chen<sup>1</sup> ✉

The far-from-equilibrium solidification during additive manufacturing often creates large residual stresses that induce solid-state cracking. Here we present a strategy to suppress solid-state cracking in an additively manufactured AlCrFe<sub>2</sub>Ni<sub>2</sub> high-entropy alloy via engineering phase transformation pathway. We investigate the solidification microstructures formed during laser powder-bed fusion and directed energy deposition, encompassing a broad range of cooling rates. At high cooling rates ( $10^4$ – $10^6$  K/s), we observe a single-phase BCC/B2 microstructure that is susceptible to solid-state cracking. At low cooling rates ( $10^2$ – $10^4$  K/s), FCC phase precipitates out from the BCC/B2 matrix, resulting in enhanced ductility (~10 %) and resistance to solid-state cracking. Site-specific residual stress/strain analysis reveals that the ductile FCC phase can largely accommodate residual stresses, a feature which helps relieve residual strains within the BCC/B2 phase to prevent cracking. Our work underscores the value of exploiting the toolbox of phase transformation pathway engineering for material design during additive manufacturing.

Laser-powder-based additive manufacturing (AM) techniques are frequently used to fabricate metals and alloys owing to their unique ability to produce parts with complicated geometries<sup>1</sup>. These methods can be further delineated into laser powder-bed fusion (L-PBF) and laser-directed energy deposition (L-DED). In L-PBF, a bed of powders is spread over a printing substrate and a highly focused laser melts the powders based on a custom computer-aided design (CAD). In L-DED, an inert carrier gas is used to blow the powders through a nozzle while being melted simultaneously by a laser. Both techniques employ a highly focused laser with a small beam size to melt feedstock powders to manufacture parts layer by layer<sup>2</sup>. The high energy input and highly transient laser-powder interactions during laser AM induce high thermal gradients and solidification rates. L-PBF tends to achieve cooling rates of approximately  $10^4$ – $10^6$  K/s and L-DED typically

achieves cooling rates of  $10^2$ – $10^5$  K/s<sup>3–5</sup>. As a result, highly non-equilibrium microstructures can develop upon rapid solidification of AM<sup>6–8</sup>. In this study, we leverage the combination of these two techniques to vary the cooling rate over several orders of magnitude to build a more complete understanding of the effects of cooling rate on solidification microstructure and mechanical properties of additively manufactured metal alloys.

The formation of many undesirable processing defects including keyholes, lack of fusion (LOF) pores, and cracking often cause severe degradation of the mechanical properties of additively manufactured materials<sup>9–12</sup>. LOF defects form as a result of insufficient energy input, leading to incomplete adhesion of adjacent layers<sup>13,14</sup>. Keyholes arise when excessive heat is applied and some low melting-point metal constituents may rapidly vaporize during printing, leading to the formation of trapped

<sup>1</sup>Department of Mechanical and Industrial Engineering, University of Massachusetts, 160 Governors Dr., Elab 317, Amherst, MA 01003, USA. <sup>2</sup>Department of Microstructure Physics and Alloy Design, Max-Planck-Institut für Eisenforschung GmbH, Max-Planck-Straße 1, 40237 Düsseldorf, Germany. <sup>3</sup>Department of Mechanical Engineering, National University of Singapore, Singapore 117575, Republic of Singapore. <sup>4</sup>Department of Mechanical, Materials, and Aerospace Engineering, Illinois Institute of Technology, Chicago, IL 60616, USA. <sup>5</sup>Division of Materials Sciences and Engineering, Ames National Laboratory, Ames, IA 50011, USA. <sup>6</sup>Institute of Materials Research and Engineering (IMRE), Agency for Science, Technology and Research (A\*STAR), 2 Fusionopolis Way, Innovis #08-03, Singapore 138634, Republic of Singapore. <sup>7</sup>These authors contributed equally: Shahryar Mooraj, Xizhen Dong, Shengbiao Zhang.

✉ e-mail: [sun\\_zhongji@imre.a-star.edu.sg](mailto:sun_zhongji@imre.a-star.edu.sg); [wenchen@umass.edu](mailto:wenchen@umass.edu)

gas bubbles<sup>15,16</sup>. Thus, porosity of a printed part can be minimized by adjusting the energy input to minimize vaporization and maximize metallic bonding between adjacent print tracks and layers. The repeated thermal cycling during AM can induce high residual stresses in as-printed materials<sup>17</sup>. Moreover, some materials experience a significant drop in ductility upon cooling after rapid solidification<sup>18</sup>. As such, many materials are particularly vulnerable to cracking, which is often distinguished into two types: solidification cracking (also known as hot cracking or hot tearing) and solid-state cracking (also referred to as cold-cracking)<sup>19</sup>. Hot cracks occur at high temperatures near the end of the solidification process and form in the mushy zone when insufficient liquid backfilling occurs in the intergranular region of the mushy zone. These cracks are often found at high angle grain boundaries (HAGBs) parallel to the solidification growth direction and are thus parallel to the build direction in additively manufactured materials<sup>10,20,21</sup>. Reducing the solidification range and grain size have proven effective to mitigate hot cracking<sup>22–24</sup>. In addition, previous studies such as those carried out by Sun et al.<sup>25</sup> and Niu et al.<sup>26</sup> employed microalloying as an effective means to engineer grain boundary segregation and phase transformation to mitigate hot cracking. While porosity and hot cracking have been extensively studied in many additively manufactured materials, there are fewer studies on the mitigation of solid-state cracking (i.e., cold cracking)<sup>27,28</sup>. Solid-state cracks occur at lower temperatures in the already solidified regions due to the limited ductility of the material, especially under the combined effect of substantial thermal residual stresses from AM processes<sup>19</sup>. Solid-state cracks are often significantly larger than the melt-pool size. Unlike hot cracking, solid-state cracking can exhibit transgranular propagation with many sharp kinks that may not align with the build direction<sup>19</sup>. Previous studies have attempted to use pre-heating to reduce residual stresses and, consequently, mitigate solid-state cracking during AM<sup>17</sup>. However, this strategy often requires high pre-heating temperatures (e.g., ~700 °C), significantly increasing the energy costs of the AM process<sup>17,29</sup>. Alternatively, some researchers have employed alloy design to reduce residual stresses during AM. For instance, Li et al. incorporated a Cu-Ni alloy into a Fe-based bulk metallic glass (BMG) during L-PBF to form a BMG matrix composite with a secondary crystalline phase<sup>30</sup>. They observed that the crystalline phase underwent plastic deformation during L-PBF, aiding in the release of thermal stresses in the BMG matrix and preventing cracking during AM<sup>30</sup>. Nevertheless, the alloy design approach for crack mitigation is inherently complex and practically challenging due to the far-from-equilibrium microstructure and phase evolution during AM.

Unlike many conventional alloy systems designed based on a single principal element, high-entropy alloys (HEAs) or multi-principal element alloys offer a vast design space with numerous possible compositions and phases for new materials development<sup>31–33</sup>. Atomic diffusion in HEAs is often slower than that in traditional dilute alloys<sup>34</sup>. The high entropy of mixing and sluggish diffusion frequently promote the formation of metastable solid solution phases at high cooling rates, which can subsequently decompose into more stable phases upon heat treatment<sup>35,36</sup>. This underscores the significance of thermal history in the phase selection of HEAs and suggests opportunities to use processing as a toolbox for tuning the phase transformation pathway to modulate the microstructure and mechanical properties of HEAs. These characteristics of HEAs make them ideal candidates for studying the effect of AM processing conditions and for achieving a wide breath of microstructure, phases content, and mechanical properties within the same alloy system, which has been rarely reported for traditional alloy systems.

Here, we present a strategy to suppress solid-state cracking by controlling the AM process and tuning the thermal history and phase transformation pathway during the AM of multi-component metal alloys. Using AlCrFe<sub>2</sub>Ni<sub>2</sub> (molar ratio) HEA as an exemplary system, we printed samples using both L-DED and L-PBF techniques, covering a wide range of cooling rates by varying the laser scan speed (*V*). This alloy shows remarkably different microstructures compared to results found in literature when printed under difference scan speeds<sup>39,37–40</sup>. These novel microstructures suggest the AlCrFe<sub>2</sub>Ni<sub>2</sub> alloy is particularly sensitive to processing

conditions of AM. Such high sensitivity makes this alloy ideal to study the complex interplay between thermal history, cooling rate, solidification microstructure, and solid-state phase transformations in HEAs under AM conditions. The L-PBF samples consist of B2/BCC (body-centered cubic) phase and exhibit severe solid-state cracks. This cracking mechanism is far less explored in literature compared to solidification cracking that occurs at elevated temperatures near the melting point of alloys as illustrated in previous studies of other additively manufactured HEAs<sup>25,41,42</sup>. As previously mentioned, typical solutions to the issue of solid-state cracking rely either on expensive pre-heating conditions or complex alloy design to avoid unfavorable phases. This work offers a unique pathway to design the phase content of an alloy by tuning the heating and cooling rates during AM and engineering the phase transformation pathway. The method presented allows the access to a wide variety of solidification microstructures and mechanical properties within the same alloy without the need for complex alloy design and thus offers a streamlined path to achieve high performance additively manufactured metal alloys.

In comparison to the L-PBF samples, the L-DED samples, with lower cooling rates, are crack-free and contain a multi-phase structure comprising FCC (face-centered cubic) and BCC/B2. Through systematic microstructural characterization, thermal modeling, thermodynamic and kinetic considerations of phase evolution, and site-specific residual stress/strain analysis, we reveal that the mitigation of solid-state cracking in the L-DED samples arises from a solid-state transformation of BCC/B2 into FCC in the heat-affected zone (HAZ), alleviating residual stress buildup in the brittle BCC/B2 phase. In addition, among the L-DED samples, the FCC phase fraction continuously increases with decreasing cooling rate, enabling a broad range of mechanical properties. Combining the experimental and modeling analyses, we unveil that the high cooling rate of L-PBF kinetically suppresses the formation of the FCC phase. On the other hand, the lower cooling rate during L-DED promotes elemental diffusion, allowing for the nucleation and growth of the FCC phase in the HAZ. Our work provides a novel route to suppress solid-state cracking and achieve controlled microstructures and properties for additively manufactured metal alloys by tuning the phase transformation pathway during AM. The ability to precisely control the solidification microstructure of the as-printed alloy offers a unique opportunity to tailor the mechanical properties of the material as needed for various applications. This finding is particularly encouraging for AM of crack-free, high-performance parts of certain multi-component metal alloys which are sensitive to the cooling rate and thermal cycling, where complex phase selection evolves during the non-equilibrium AM process.

## Results and discussion

### Microstructure and phase analysis

The overarching goal of this work is to explore a new strategy for mitigating solid-state cracking by engineering the phase transformation pathway and residual stresses during AM. The AlCrFe<sub>2</sub>Ni<sub>2</sub> HEA was selected for this study as it is known to undergo severe solid-state cracking as opposed to solidification cracking under L-PBF conditions but also shows a dual-phase FCC/BCC microstructure under casting conditions<sup>29,39</sup>. This suggests the microstructure of the alloy may be highly sensitive to the thermal history during processing and thus may be tuned by manipulating the thermal history and cooling rate during AM. To this end, we employ both L-DED and L-PBF techniques, enabling access to a wide range of cooling rates by primarily varying the laser scan speed. Figure 1 shows the optical micrographs of the L-PBF and L-DED samples taken from the middle of the printed plates. In the L-PBF sample, no obvious microstructural features are visible, but zig-zagged cracks are frequently observed (Fig. 1a). These cracks are notably longer than the melt pool width and exhibit a transgranular propagation behavior, with orientations roughly perpendicular to the build direction. Furthermore, these cracks feature sharp kinks, in contrast to typical hot tears (or hot cracks) that often form along the building direction at high angle grain boundaries (HAGBs)<sup>42</sup>. Unlike intergranular hot cracks, solid-state cracking can show transgranular propagation and can easily

reach lengths substantially larger than the melt pool in AM<sup>43</sup>. These distinctions allow one to distinguish between solid-state cracking and hot cracking. The presence of abundant solid-state cracks suggests a buildup of high residual stresses and/or the brittleness of the L-PBF sample. In contrast, the L-DED samples are crack-free and exhibit a bright network of structures that seem to correspond to a secondary phase (Fig. 1b–d), which will be discussed later. The dashed blue lines in Fig. 1a–d illustrate the melt pool boundary in each sample. Of particular interest, the melt pool interior of these L-DED samples shows a homogeneous contrast, suggesting a nearly single-phase microstructure, while the HAZ clearly exhibits a dual-phase pattern. The secondary phase becomes increasingly coarser and denser in the HAZ as the laser scan speed decreases. Since the HAZ only experiences re-heating (without remelting) by subsequent laser tracks, the occurrence of a secondary phase primarily in the HAZ, as opposed to the interior of the melt pool, implies that this secondary phase arises largely due to solid-state phase transformation rather than solidification (i.e., liquid → solid transformation). Such observations imply that the cyclic heating/cooling (i.e.,

in situ thermal cycling) during layer-by-layer printing causes nucleation of the secondary phase in the L-DED samples. Multiple thermal cycles kinetically favor the diffusion of elements, encouraging the growth of the secondary phase.

Notably, some HAZ regions in AM materials may overlap with the melt pool of the preceding layer. To confirm whether the formation of the secondary phase in the HAZ arises from thermal-cycling-induced solid-state transformation or from solidification in the melt pool of the preceding layer, we further examined the microstructure of the top print layer of each sample. Consistently, the L-PBF sample shows marked cracking with no secondary phase (Fig. 2a), whereas the L-DED samples exhibit no cracking with a nearly single-phase microstructure within the melt pool but dual phases in the HAZ (Fig. 2b–d). Close-up views of the melt pool interior and HAZ regions in these samples are shown in Fig. 2e–h. These observations further corroborate our speculation that the secondary phase is formed during solid-state phase transformation within the HAZ rather than during the liquid solidification process. The XRD patterns reveal that the L-PBF sample is only comprised of BCC/B2 phase (see Fig. 3 black line). On the other hand, the L-DED samples contain a secondary FCC phase, and the relative peak intensity (i.e., volume fraction) of the FCC phase increases with decreasing laser scan speeds. These findings imply that the secondary phase observed under optical microscopy corresponds to the FCC phase.

Next, we investigated the grain morphology, grain size, and phase distribution through electron backscatter diffraction (EBSD) analysis. EBSD images were all taken from the center of each sample to ensure a similar number of thermal cycles for each sample. Figure 4a–d show the inverse pole figure (IPF) maps and phase maps superimposed on image quality (IQ) maps for both L-PBF and L-DED samples. The L-PBF sample exhibits a single BCC/B2 phase, while the L-DED samples contain dual phases of both BCC/B2 and FCC, consistent with the XRD results. In the L-DED samples, the FCC phase forms in the HAZ close to the boundary of the melt pool. Furthermore, the fraction of the FCC phase increases as the laser scan rate decreases from 6.2 mm/s to 3.3 mm/s. Typically, a smaller scan speed causes a slower cooling rate and, consequently, a larger grain size after solidification. However, a surprising opposite trend is observed here. The L-PBF sample with the highest scan speed shows the largest average BCC/B2 grain size, while the L-DED samples exhibit a decreased average BCC/B2 grain size when the scan speed decreases. The statistical data retrieved from the EBSD IPF maps are summarized in Fig. 4e. As the amount of the BCC/B2 phase decreases from 100 vol.% (L-PBF,  $V = 375$  mm/s) to 52 vol.% (L-DED,  $V = 3.3$  mm/s), the average BCC/B2 grain size drastically drops from  $\sim 139$   $\mu\text{m}$  to  $\sim 23$   $\mu\text{m}$ . The EBSD phase maps in Fig. 4a–c suggest that many

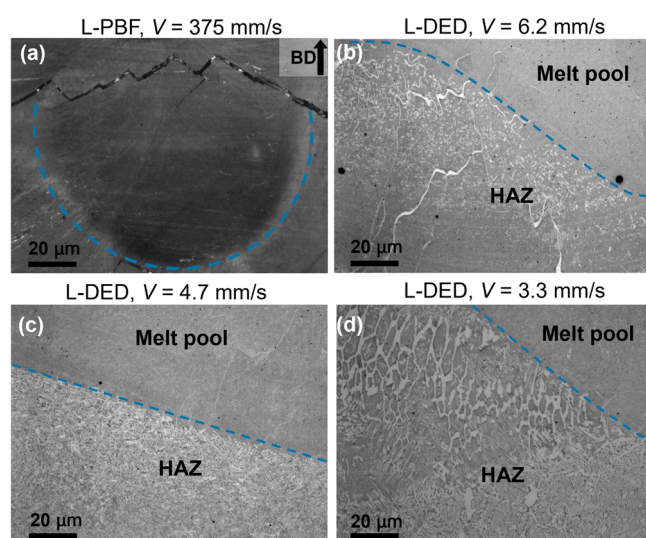


**Fig. 1** | Optical micrographs of samples with different printing conditions. Melt pool boundaries are marked with dashed blue lines. **a** L-PBF,  $V = 375$  mm/s. The arrow shows the build direction (BD), **b** L-DED,  $V = 6.2$  mm/s, **c** L-DED,  $V = 4.7$  mm/s, **d** L-DED,  $V = 3.3$  mm/s.

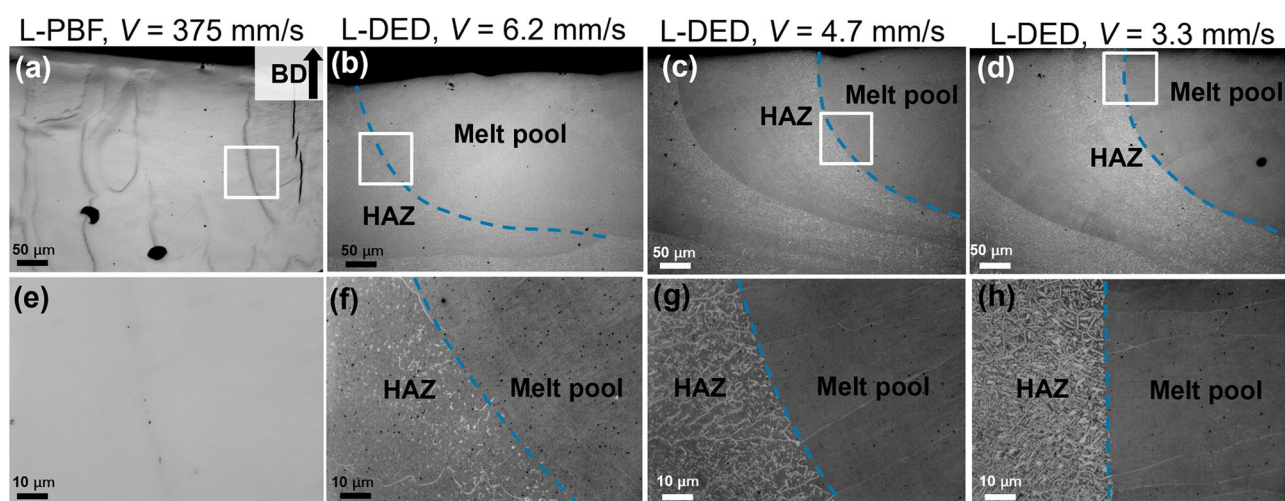


**Fig. 2** | Optical micrographs of the top layer of samples with different printing conditions. Melt pool boundaries are marked with dashed blue lines. **a** L-PBF,  $V = 375$  mm/s. The arrow shows the build direction (BD), **b** L-DED,  $V = 6.2$  mm/s,

**c** L-DED,  $V = 4.7$  mm/s, **d** L-DED,  $V = 3.3$  mm/s. The white box indicates the region of the high-magnification image for each sample shown in **e–h**.



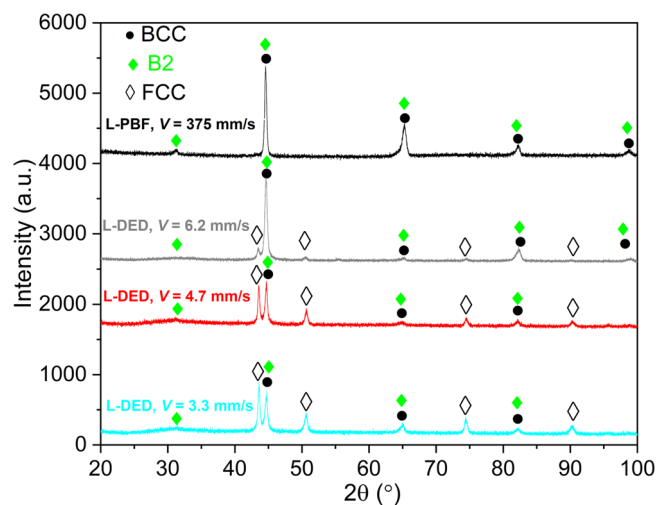


**Fig. 3 | XRD patterns of the L-DED and L-PBF samples.** These XRD patterns show different phase constituents under different printing conditions.

FCC grains nucleate and grow at the BCC/B2 grain boundaries. Thus, the steady growth of FCC grains and the increase in their volume fraction result in continuous annihilation of the BCC/B2 phase and reduction in its average grain size. Figure 4 also shows a clear change in the texture between samples processed under different laser scan speeds. This change in texture likely arises from the changes in thermal gradients and cooling rates at different printing conditions. The introduction of secondary FCC phase helps interrupt the epitaxial growth of the parent BCC/B2 phase, leading to reduced texture as the laser scan speed decreases.

To further understand the crack mitigation mechanism in the L-DED samples, we investigated the EBSD micrographs of these samples at higher magnification to better resolve the secondary FCC phase. As shown in Fig. 5, the FCC grains mainly manifest in two morphologies. They either appear as continuous lines following the trajectory of the parent BCC/B2 grain boundaries, or they take the form of acicular precipitates inside the BCC/B2 grains. Due to the higher atomic packing density of the FCC (0.74) structure compared to the BCC (0.68) structure, the transformation from BCC/B2 to FCC induces a volumetric shrinkage and introduces residual stresses/strains. This is confirmed by the corresponding Kernel Average Misorientation (KAM) maps, showing significant increases in KAM values in both BCC/B2 and FCC phases with increasing FCC phase fractions (Fig. 5c, g, k). The FCC grains are visible within the scanning electron microscopy (SEM) images (Fig. 5d, h, l), consistent with the results from the phase maps (Fig. 5b, f, j). The FCC phase appears to preferentially precipitate along the parent grain boundaries first, as the individual acicular secondary phase only starts to fill up the BCC/B2 grain interiors after their grain boundaries are fully occupied by the FCC phase (Fig. 5b, f, j). This observation suggests that the parent BCC/B2 grain boundaries are favored locations for solid-state phase transformation, presumably due to higher local defect densities and associated chemical segregation<sup>44</sup>. Interestingly, a close-up view of the microstructure of a typical L-DED sample under SEM reveals that the BCC/B2 regions feature a nanoscale intertwined characteristic (Fig. 6), reminiscent of the classical bi-continuous feature after spinodal decomposition<sup>45</sup>. Note that spinodal decomposition has been reported in several Al-(Co)-Cr-Fe-Ni HEAs<sup>46,47</sup>. The interfaces of the chemically modulated BCC and B2 regions can act as preferential sites for nucleation of the FCC phase owing to its local elastic strain energy (coherency stress), which serves as a driving force for the solid-state nucleation of the FCC crystallite inside the BCC/B2 phase<sup>29,48</sup>.

### Mechanical properties

Figure 7a presents the tensile properties of the three L-DED samples. Each condition was tested three times, and representative curves are presented in

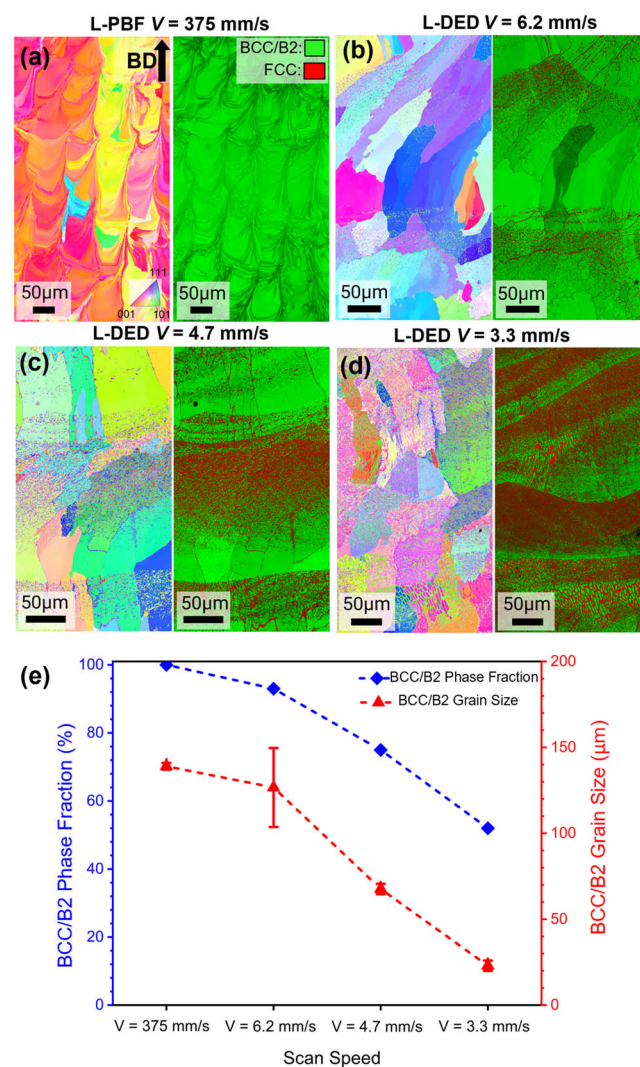


**Fig. 4 | EBSD IPF maps and phase maps superimposed with IQ maps of considered samples.** **a** L-PBF,  $V = 375$  mm/s. The arrow shows the build direction (BD), **b** L-DED,  $V = 6.2$  mm/s, **c** L-DED,  $V = 4.7$  mm/s, **d** L-DED,  $V = 3.3$  mm/s, **e** BCC/B2 phase fraction and average BCC/B2 grain size for different types of samples. The EBSD images were all taken near the center of the samples to ensure the samples reflected the effect of a similar number of thermal cycles between the L-DED samples.

this work. It is important to note that the severe solid-state cracking in the L-PBF sample caused premature failure in the elastic regime, and hence, the result is not shown. Among the L-DED samples, we observe a remarkable increase in tensile elongation (or fracture strain) from 2.2% to 10.3% with a decrease in the scan speed from 6.2 mm/s to 3.3 mm/s, accompanied by a reduction in yield strength from 1120 MPa to 960 MPa. This evolution of mechanical properties is linked to the increase in FCC phase fraction, as the FCC structure is typically more ductile and softer than the BCC/B2 structure. The wide range of strength-ductility combinations across different L-DED samples highlights ample opportunities to readily tune the properties of the AlCrFe<sub>2</sub>Ni<sub>2</sub> HEA system by engineering the laser printing protocol.

Figure 7b–e shows the surface morphologies of fractured samples. The fracture surface of the L-PBF sample appears smooth and flat with cleavages indicative of brittle fracture (Fig. 7b). The cleavages suggest catastrophic failure due to transgranular cracking, common in brittle materials. The fracture surface of the L-DED sample with  $V = 6.2$  mm/s has a mixed feature of dimples and flat cleavages, suggesting a combination of ductile and brittle fracture modes (Fig. 7c). Figure 7d, e displays the L-DED samples with further reduced scan speeds of  $V = 4.7$  mm/s and 3.3 mm/s, respectively.

**Fig. 5 | High-resolution EBSD images of the L-DED samples.** a–d IPF map, phase map superimposed on the IQ map, KAM map, and SEM image of the L-DED,  $V = 6.2$  mm/s sample, respectively. e–h same as a–d but for L-DED,  $V = 4.7$  mm/s sample. i–l same as a–d but for L-DED,  $V = 3.3$  mm/s sample.

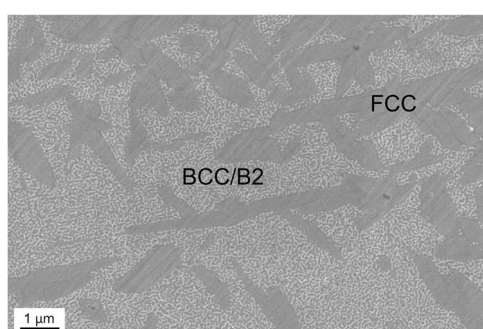
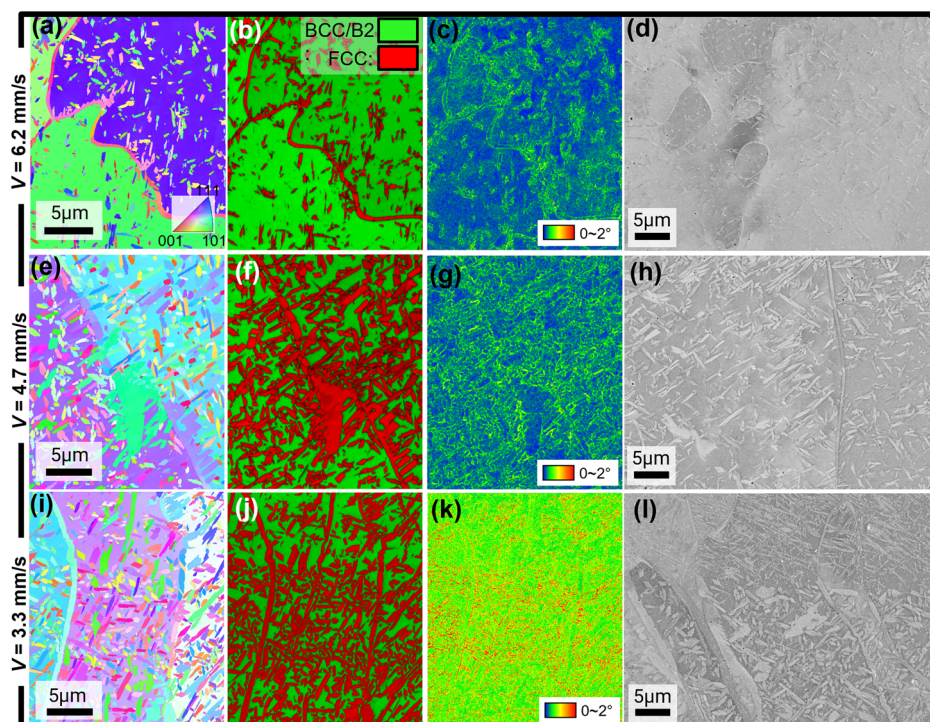


**Fig. 6 | SEM micrograph of the etched L-DED,  $V = 3.3$  mm/s sample.** Spinodal-decomposition-like features were observed in the BCC/B2 regions. A similar morphology was also observed in other L-DED samples (not shown here).

Both samples exhibit ductile features with massive dimple patterns, which occur often due to micro-void coalescence during plastic deformation, as opposed to catastrophic cleavage in brittle materials. These results exemplify the immense role of phase fraction and microstructure in the mechanical performance of this alloy through controlled precipitation of a secondary FCC phase. Thus, consideration of the phase transformation pathway is crucial to designing additively manufactured alloys with desired properties for specific applications.

The above observations indicate that the nucleation and growth of the FCC phase within the BCC/B2 structure helps postpone the onset of fracture instability. To understand the impact of the secondary FCC phase on crack propagation, we examined the gauge section of the fractured specimen with the largest ductility (L-DED,  $V = 3.3$  mm/s). Figure 8a shows a typical signature of crack propagation from the edge towards the center of the side surface. Notably, the crack is initiated on the rough outer surface and propagates through the BCC/B2 region; however, its growth is deflected and arrested when it encounters the dual-phase area of FCC + BCC/B2 (Fig. 8b). It is widely understood that the FCC phase often achieves much higher ductility than the BCC/B2 phase, given that the FCC structure has a higher amount of close-packed slip planes compared to those in the BCC/B2 phase.

Since the FCC crystallite can accommodate a large plastic strain compared to the BCC/B2 phase, the stress concentration at the crack tip can be reduced as the crack tip blunts via plastic deformation of the FCC grains. This release of stress concentration at the crack tip helps delocalize the plastic strain, making the alloy more resistant to crack propagation with an overall enhanced tensile ductility. To further understand the distinct crack propagation behaviors of the L-PBF and L-DED samples, micro-indentation scratch tests were also performed (Supplementary Fig. 1). The representative morphologies of the scratch grooves are summarized in Supplementary Fig. 2, where it is seen that the L-PBF sample shows an array of parallel, semi-circular cracks densely distributed along the scratch direction, largely due to the intrinsic brittleness of the BCC/B2 phase in this sample. In contrast, the L-DED samples exhibit significantly less cracks and the crack propagation behavior is fundamentally different. The crack growth in the L-DED samples tends to be deflected and arrested when the crack encounters the dual-phase region of FCC + BCC/B2, which is generally consistent with the crack propagation pathway observation in the tensile specimen after fracture.

### Thermal history and phase transformation pathway

The solidification microstructure and mechanical behavior of additively manufactured materials depend heavily on the thermal history<sup>49,50</sup>. During laser AM, the material experiences multiple thermal cycles due to multiple adjacent laser scans within the same layer and repeated heating when building subsequent layers. The different printing techniques and scan speeds explored in this work conceivably lead to different thermal histories. In the present work, we performed finite element simulation to reproduce the influence of printing protocol on the thermal history of each sample, with the thermophysical properties used for simulation presented in Table 1.

Figure 9a, b illustrates the respective thermal cycle curves for the L-PBF and L-DED samples, which are extracted from a single point of interest (POI) schematically illustrated in Fig. 9d. The inset of Fig. 9a shows individual thermal cycles for the L-PBF sample from consecutive laser passes during the printing of the first layer. As the laser tracks approach the POI, the peak temperature increases until a maximum peak temperature is reached when the laser passes directly above the POI. The temperature then decreases as the laser tracks move away from the POI to print the rest of the layer. For the L-PBF sample, there is a fixed delay between the deposition of



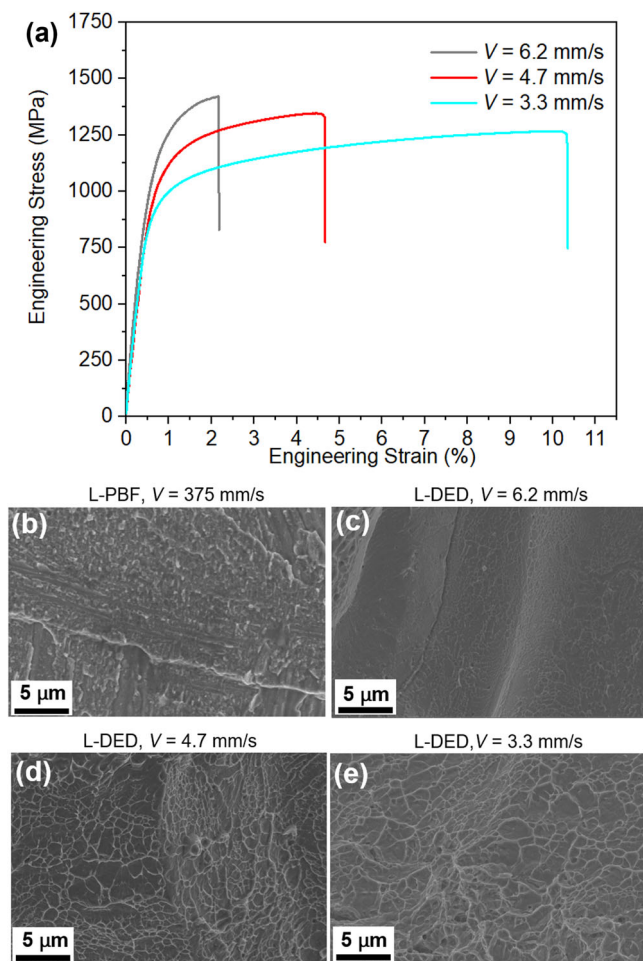


**Fig. 7 | Tensile properties and fracture surface morphologies of different samples.** a Engineering stress-strain responses of considered L-DED samples. Note that the L-PBF sample ( $V = 375$  mm/s) was also tested but failed prematurely in the elastic regime due to existence of many solid-state cracks. The tensile curves of the L-PBF specimens are not reproducible and hence not shown. b–e SEM micrographs of the fractured surfaces of different samples. b L-PBF,  $V = 375$  mm/s, c L-DED,  $V = 6.2$  mm/s, d L-DED,  $V = 4.7$  mm/s, e L-DED,  $V = 3.3$  mm/s.

consecutive layers, corresponding to the time needed to re-coat a new layer of powders. This delay leads to a time gap between the individual thermal patterns of consecutive layers. The thermal cycles experienced by the L-DED samples shown in Fig. 9b exhibit a similar trend to the thermal cycles of the L-PBF sample. The peak temperature increases for each laser track until a maximum peak is achieved when the laser passes above the POI, then the temperature decreases as the rest of the layer is printed. The inset within Fig. 9b shows that the shape of the thermal cycles is less sharp, and the drops between subsequent peak temperatures are also much smaller than those in L-PBF sample. The shape of these peaks suggests that the cooling rates are much lower in L-DED samples. The diffusion of elements usually increases with temperature. Thus, when other conditions are similar, a lower cooling rate allows the sample to be maintained at elevated temperatures for longer periods, resulting in longer diffusion lengths. Figure 9c shows the cooling rate for each type of sample after the laser moves directly over the POI. The data points in this plot serve as a relative comparison of the cooling rates among different samples under different printing conditions. A more detailed analysis of the site-specific cooling rates within each sample is discussed later in this section. Notably, the cooling rates of the samples produced by L-DED are around two orders of magnitude lower than the sample produced by L-PBF. Furthermore, decreasing the scan speed also causes a lower cooling rate, kinetically facilitating the solid-state phase

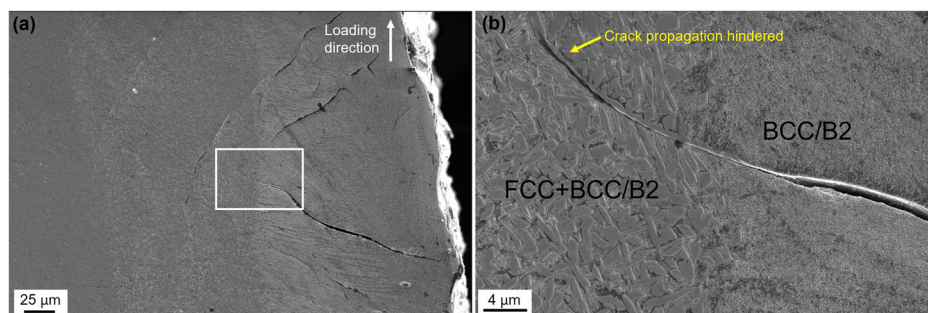
transformation from the BCC/B2 phase to the FCC phase. Figure 9d presents a typical optical micrograph of an experimental melt pool of the L-DED,  $V = 3.3$  mm/s sample compared with the simulated cross-section of a melt pool for the same printing condition to verify the accuracy of the simulation. The white dotted line outlines the shape of the simulated melt pool, while the black dotted line illustrates the melt pool boundary of the experimental melt pool. Although the as-printed melt pool does not assume a hemi-spherical shape as shown in the simulation, the depth and width of the as-printed melt pool are close enough to those in the simulation for reasonable comparisons.

Figure 10a–d illustrates the differences in temperature distribution in the melt pool and HAZ, as well as the variations in melt pool size when the heat source passes over the POI for different samples. Figure 10e shows the cooling rates at different locations below (negative values) and above (positive values) the melt pool boundary. We observe that the sample produced by L-PBF experiences the largest cooling rate, and this drops significantly in the L-DED samples with decreasing scan speed. Within each sample, the cooling rate decreases from the melt pool surface through the boundary of the melt pool to the HAZ. These results help rationalize the experimental observations that the FCC phase is kinetically suppressed in the melt pool during the rapid solidification of either the L-PBF or L-DED process. Additionally, it is also suppressed in the HAZ of the L-PBF sample, as the cooling rate during thermal cycling remains too high to allow for the nucleation of the FCC structure. On the other hand, HAZs of L-DED samples experience smaller cooling rates, which facilitate the precipitation of the secondary FCC phase.

The thermal history can kinetically affect the phase transformation pathway in laser additively manufactured materials. As mentioned earlier, a high cooling rate can largely suppress atomic diffusion and promote polymorphic or diffusionless solidification, preventing the precipitation of the secondary phase. To conceptually understand the impact of varying cooling rates on the phase transformation pathway, one may adopt a continuous cooling transformation (CCT) diagram<sup>51</sup>. This diagram illustrates the correlation between the thermal history of a material and the formation of phases by depicting the starting and finishing temperatures for a given phase transformation measured at constant cooling rates<sup>52</sup>. Figure 11a schematically illustrates a CCT diagram for the AlCrFe<sub>2</sub>Ni<sub>2</sub> alloy, presenting the correlation of cooling rate with the fraction of a secondary phase. The shapes and positions of the transformation start and finish curves depend on the solid-state diffusion length, which controls the growth of nuclei of the secondary phase, and the rate at which critical nuclei form during cooling (also known as the nucleation rate). Specifically, a very fast laser scan speed leads to a high cooling rate, preventing the precipitation of the FCC phase because the time-temperature curve bypasses the transformation start curve for FCC nucleation. This implies that the generation of critical nuclei of the FCC phase is mostly suppressed, resulting in purely B2/BCC phase, as observed in the L-PBF sample. In contrast, a slower cooling rate results in a temperature profile where elevated temperatures are maintained for a sufficient time to allow for FCC phase nucleation, as observed in the L-DED samples (Figs. 1 and 5). Prior literature suggests that such a BCC/B2 → FCC solid state phase transformation is a nucleation and growth process in a similar HEA (AlCoCrFeNi)<sup>53</sup>. The transformation rate and actual volume fraction of the resultant FCC phase are influenced by factors such as atomic diffusivity, interfacial energy, number density of nucleation sites, etc.<sup>54</sup>. These physical parameters are yet challenging to determine for multi-component HEAs, and a quantitative analysis of such solid-state phase transformation kinetics is worth investigating in the future.

To qualitatively examine the possible phase transformation pathways in AlCrFe<sub>2</sub>Ni<sub>2</sub> HEA at different printing conditions, calculation of phase diagram (CALPHAD) was performed to predict equilibrium phases in relation to temperature. Figure 11b shows a calculated equilibrium phase diagram via Thermocalc, which was also used to generate the liquidus and solidus temperatures used in thermal modeling. According to the equilibrium phase diagram, both the FCC and BCC phases form at a similar temperature around 1269 °C after solidification. It should be noted that the

**Fig. 8 | SEM micrograph of the fractured side surface of the L-DED,  $V = 3.3$  mm/s sample, showing the effect of the secondary FCC phase on the crack propagation during deformation.** a Low-magnification image near the edge of the side surface. The white box indicates the region corresponding to the high-magnification image in b. b High-magnification image illustrates that crack propagation in the BCC/B2 is deflected and hindered once the crack encounters the dual-phase region of FCC and BCC/B2.



equilibrium nature of the calculated phase diagram does not include the details on the kinetics of the phase transformation. Thus, it is difficult to understand the rate at which each phase forms and to interpret the order in which different phases form. Nonetheless, our multifaceted material characterization results from optical microscopy, XRD, and EBSD show that the L-PBF sample is comprised of only BCC/B2. This discrepancy indicates that nucleation of the FCC phase is kinetically inhibited. While there are certainly prior examples of kinetic suppression of the secondary phase in the L-PBF process<sup>51</sup>, the equilibrium phase diagram in Fig. 11b helps explain why the FCC is suppressed in our work. This diagram shows that the B2 phase forms first at a higher temperature than both the BCC and FCC phases, which form later at lower temperatures.

Figure 11c–e shows the equilibrium mole fractions of different constituent elements in each phase, illustrating the importance of complex elemental partitioning to form FCC and BCC phases from the higher-temperature phase of B2 after solidification. Specifically, the FCC phase is expected to be rich in Fe, while the B2 phase is rich in Ni and Al, and the BCC phase is rich in Cr. Therefore, faster cooling rates during L-PBF substantially suppress atomic diffusion and promotes solute trapping within the B2 phase. As a result, the secondary FCC phase cannot nucleate either in the melt pool during solidification (liquid → solid) or in the HAZ upon subsequent thermal cycling (solid → solid). However, note that the B2 phase can often undergo spinodal decomposition during solidification to form a chemically modulated structure containing ordered B2 and disordered BCC<sup>29,44</sup>. Spinodal decomposition is a phase transformation process with no nucleation barrier and is driven by the free energy change of minor compositional fluctuations throughout the material. Thus, it only requires diffusion at a short-range distance (on the order of angstroms to nanometers), which allows the B2 phase to decompose into BCC/B2 despite the rapid cooling rate<sup>29,44</sup>. In fact, spinodal decomposition of an ordered B2 phase into a BCC/B2 structure has been predicted by thermodynamic calculations of

other HEAs which showed that the B2 ordered phase has a lower Gibbs free energy than the disordered BCC phase<sup>55,56</sup>. The presence of such spinodal structures has also been experimentally verified in such studies<sup>55,56</sup>.

In contrast, the development of the secondary FCC structure relies on the nucleation of FCC grains that requires a large cluster of atoms to form the specific crystallographic structure and composition (Fig. 11e)<sup>37</sup>. Hence, the solid-state transformation of BCC/B2 to FCC requires long-range diffusion (above nanometer scale), which relates to the size of critical nuclei required for growth of the FCC phase and the diffusion length across the interface of B2/BCC phase and the FCC nucleus. Thus, the formation of sufficiently large nuclei of FCC crystallites and the growth of such crystallites are only possible in the HAZ of the L-DED samples where the cooling rates are much lower to allow for significant diffusion during thermal cycling (Fig. 10e). For example, SEM electron dispersive X-ray spectroscopy (EDS) maps of the L-DED,  $V = 3.3$  mm/s sample in Fig. 12a show that the BCC/B2 matrix is Al- and Ni-rich, while FCC grains are rich in Fe and Cr. The chemical segregation underscores the requirement of long-range atomic diffusion to allow the precipitation of the FCC phase out of BCC/B2. It is noted that the nanoscale phase separation between BCC and B2 prevents SEM EDS from clearly distinguishing them since the interaction volumes of the incident electrons extend beyond the interfaces between the chemically modulated BCC and B2 regions. Nonetheless, such BCC/B2 spinodal decomposition can be clearly distinguished by high-resolution EDS under scanning transmission electron microscopy (STEM), as shown in Fig. 12b. This result, combined with the CALPHAD modeling, suggests that it is often difficult to suppress the formation/precipitation of BCC from B2 due to the small diffusion length scale under spinodal decomposition.

### Phase-transformation-induced residual stress/strain redistribution

As discussed earlier, the primary cause of the solid-state cracking, as demonstrated in the L-PBF sample, is the accumulation of thermal residual stresses, leading to strain localization in the brittle BCC/B2 phase. In L-DED samples, the precipitation of secondary FCC grains enables strain partitioning from the brittle BCC/B2 matrix, a feature which helps to accommodate the residual stresses/strains. This section discusses the redistribution of residual stresses/strains caused by the solid-state transformation of secondary FCC grains from the BCC/B2 phase in this AlCrFe<sub>2</sub>Ni<sub>2</sub> HEA.

We utilized cross correlation EBSD (CC-EBSD) to examine the role of the additional FCC phase on the residual strain distribution and crack mitigation. Compared to traditional residual stress measurements such as conventional XRD and destructive image correlation, CC-EBSD achieves much higher resolution and can map out the local residual stress tensor in conjunction with its location-dependent microstructure. The local residual strain tensor is extracted by correlating all diffraction patterns in a single grain to a benchmark pattern associated with the pixel with the highest indexing confidence value<sup>25,57</sup>. This analysis produces a pattern shift matrix that contains contributions of the lattice rotation and elastic strain compared with the reference point. As such, the strain distribution within each grain can be precisely mapped out. Note that it is highly improbable to detect a truly strain-free point in materials produced by AM due to the far-from-

**Table 1 | Thermophysical properties applied to simulation<sup>62–64</sup>**

Material properties	Temperature (K)	Value
Solidus temperature ( $T_s$ , K)	–	1535
Liquidus temperature ( $T_l$ , K)	–	1550
Density ( $\rho$ , kg/m <sup>3</sup> )	–	7230
Specific latent heat of melting ( $L_m$ , J/mol)	–	$10.53 \times 10^3$
Emissivity factor ( $\epsilon$ )	–	0.4
Heat transfer coefficient ( $h$ , W/(K · m <sup>2</sup> ))	–	10
Specific heat ( $c_p$ , J/(K · kg))	273	401
	1550	601
	1500	38
Thermal conductivity ( $k$ , W/(K · m))	298	25
	800	31
	1500	38
Viscosity ( $\mu$ , Pa · s)	1573	0.0067
	1773	0.0046

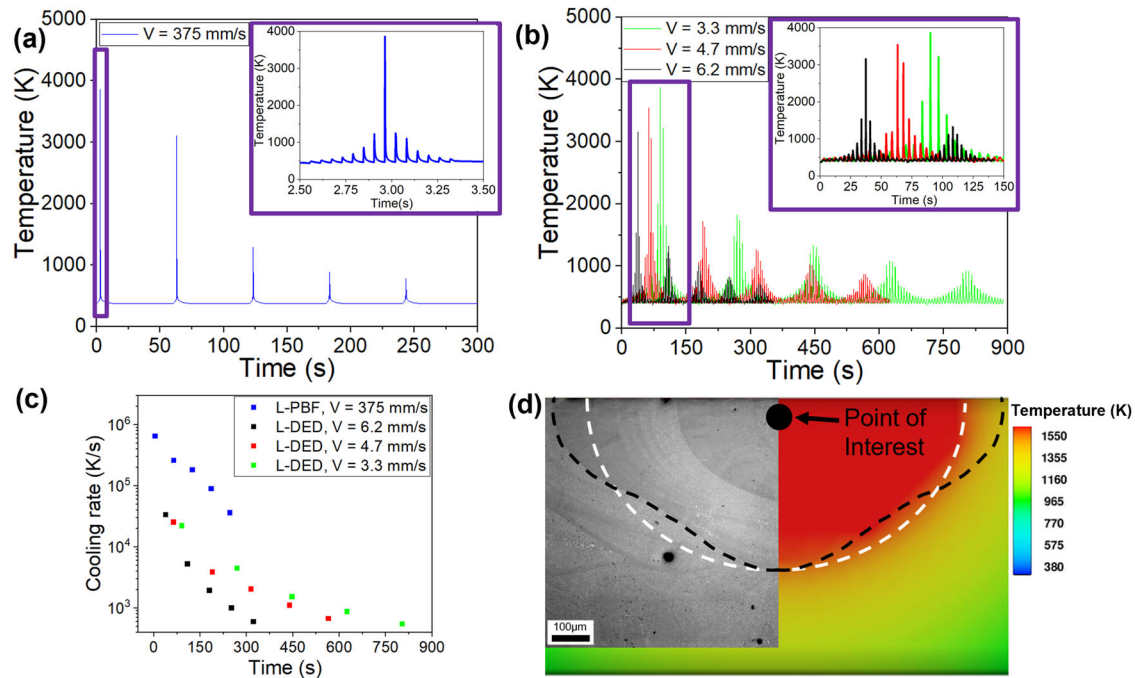


**Fig. 9 | Thermal history, temperature profile, and temporal evolution of cooling rate from finite element thermal modeling.** **a** Cyclic re-heating curves for the L-PBF sample. **b** Cyclic re-heating curves for the L-DED samples. **c** Extracted maximum cooling rate immediately after the peak temperature is reached at the POI during deposition of each layer. **d** Comparison of a cross-sectional optical

micrograph of an experimental melt pool (left) and a cross-sectional view of a simulated melt pool (right). The point of interest remains fixed even as subsequent layers are deposited on top. The white dotted line shows the melt pool boundary from simulation and the black dotted line illustrates the experimental melt pool boundary.

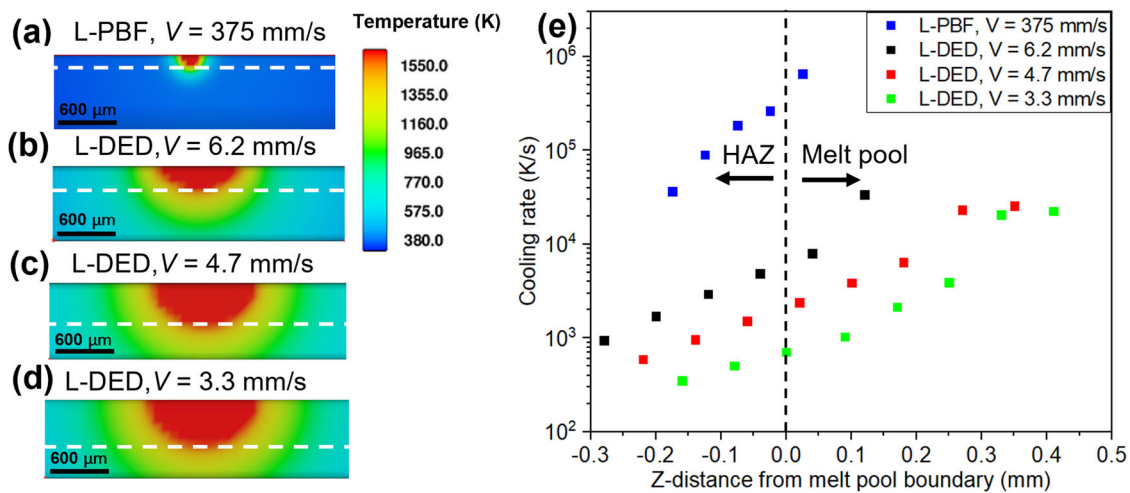


**Fig. 10 | Simulated temperature profile and cooling rate correlated to distance from melt pool boundary for each type of sample.** **a** L-PBF,  $V = 375$  mm/s, **b** L-DED,  $V = 6.2$  mm/s, **c** L-DED,  $V = 4.7$  mm/s, **d** L-DED,  $V = 3.3$  mm/s. The dashed white lines in **a–d** represent the  $z$ -position of the lower boundary of the melt pool (set

as  $z = 0$ ). **e** The simulated cooling rate measured at various  $z$ -heights from the boundary of the melt pool. Negative and positive values represent locations below and above the boundary of the melt pool, respectively. The  $x$  and  $y$  positions of these locations are set to correspond with the middle of the melt pools in **a–d**.

equilibrium thermomechanical processing conditions. Therefore, the strains presented in this work are considered relative rather than absolute measurements.

CC-EBSD study of the L-DED,  $V = 3.3$  mm/s sample was used as a representative case for the dual-phase L-DED samples. An area of  $6 \times 15 \mu\text{m}^2$  was mapped out of the sample to investigate the residual stress distribution across the multi-phase microstructure. Figure 13a shows the IPF map superimposed with the IQ map to help correlate the residual strains and the microstructural features in the sample. The distribution of residual strain tensors is depicted in Fig. 13b–d. Positive values (red color) signify

tensile strains, whereas negative values (blue color) signify compressive strains. Observing the residual strain distribution in the FCC phase (Fig. 13b–d), the FCC grains experience substantially high relative elastic strains up to 0.012. In addition, the elastic strains within the FCC grains show large strain gradients near grain boundaries, as evidenced by dotted circles in Fig. 13c. In contrast, the BCC/B2 grains show very low elastic strains, colored as light green in the CC-EBSD maps. These results suggest that the secondary FCC phase can accommodate the undesirable tensile residual stresses/strains inherent to the AM processing via large plastic deformation, hence preventing brittle BCC/B2 grains from cracking.



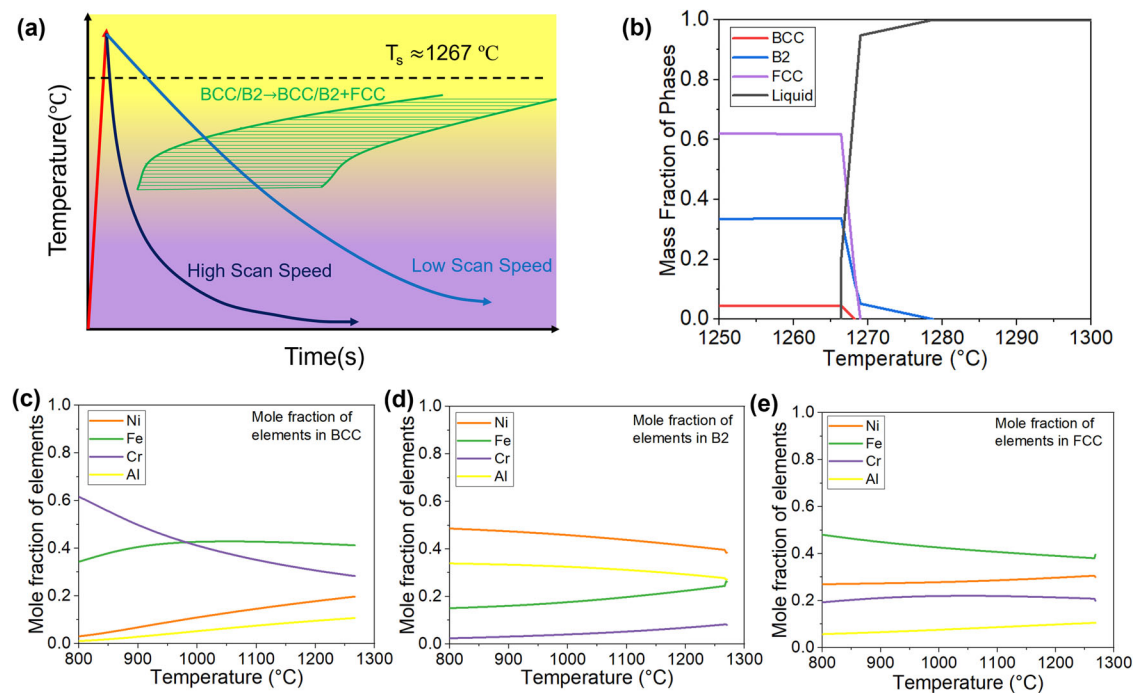


**Fig. 11 | Schematic CCT diagram, predicted phase fraction and composition by CALPHAD.** **a** Schematic illustration of the CCT diagram, showing the effect of cooling rate (or laser scan speed) on the phase transformation pathway in AlCrFe<sub>2</sub>Ni<sub>2</sub>.  $T_s$  represents the equilibrium solidus temperature of this alloy. **b** Equilibrium phase diagram showing the equilibrium phase fractions at various temperatures. **c–e** Equilibrium mole fractions of different constituent elements in different phases, i.e., BCC, B2, and FCC of the AlCrFe<sub>2</sub>Ni<sub>2</sub> HEA, respectively.

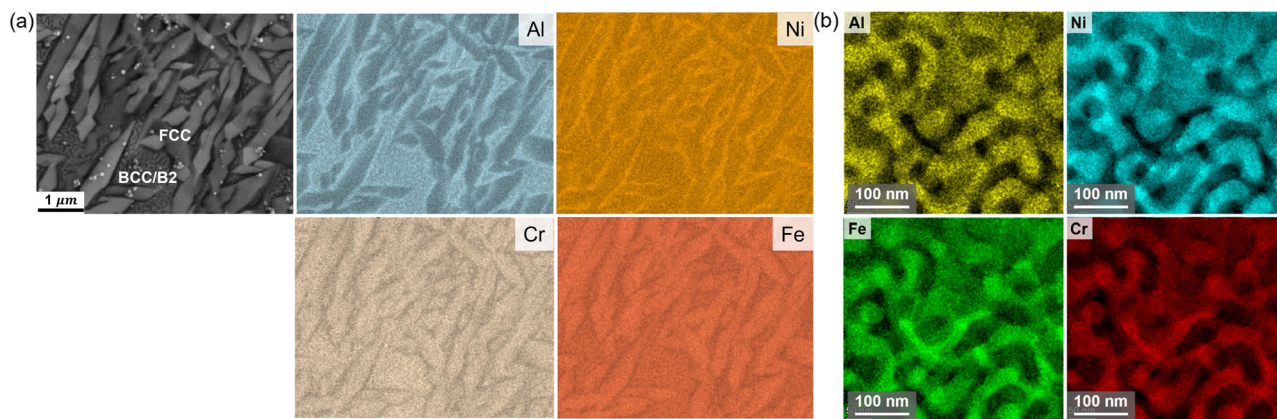


**Fig. 12 | Elemental distribution in the representative L-DED,  $V = 3.3$  mm/s sample.** **a** SEM image and EDS maps, showing segregation of elements between the FCC and BCC/B2 regions. **b** STEM EDS maps showing nanoscale spinodal decomposition in the BCC/B2 region.

The residual stress/strain distribution is also reflected in the geometrically necessary dislocation (GND) map, as seen in Fig. 13e. Similar to the elastic strains in Fig. 13b–d, the GND density in the FCC phase reaches a high value on the order of  $10^{16} \text{ m}^{-2}$ . This value is remarkably higher than the typical dislocation density of  $\sim 10^{14} \text{ m}^{-2}$  in other additively manufactured FCC alloys<sup>58,59</sup>, which highlights the extreme plastic deformations experienced by the FCC grains in the current specimen. The BCC/B2 matrix, on the other hand, only shows a GND density around  $10^{14} \text{ m}^{-2}$ , nearly two orders of magnitude below that of the FCC phase. Therefore, the majority of the accumulated residual strains have been partitioned into the FCC phase, while the BCC/B2 matrix is in a less-stressed state.

CC-EBSD measurements were also carried out on the L-PBF sample for direct comparison of the residual strain distribution. Note the severe cracking of the L-PBF sample can release residual stresses, and thus, these measured strains are believed to be underestimations of intrinsic values after solidification. These results are illustrated in Supplementary Fig. 3. The

strains measured in the L-PBF are nearly twice the strains in the L-DED sample, reaching a maximum tensile strain of 0.025 at the BCC/B2 grain boundaries. The GND density at the BCC/B2 grain boundaries also increases up to an order of  $10^{16} \text{ m}^{-2}$ . This is almost 100 times greater than the GND density measured within the BCC/B2 grains of the L-DED sample. These results highlight the vulnerability of the BCC/B2 matrix to residual stress build-up when there is no FCC phase present in the L-PBF sample. The higher thermal residual stresses make these grain boundaries more susceptible to fracture after solidification. Instead, the introduction of the ductile FCC phase can readily accommodate thermomechanical strains, reducing the residual stresses near the BCC/B2 grain boundaries for solid-state crack mitigation.

## Conclusions

In this work, we present a strategy to suppress solid-state cracking in additively manufactured metal alloys by engineering the phase

**Fig. 13 | CC-EBSD maps of the L-DED,  $V = 3.3$  mm/s sample. a** Phase map superimposed with an IQ map. **b–d** Elastic strain maps. **e** GND density map.

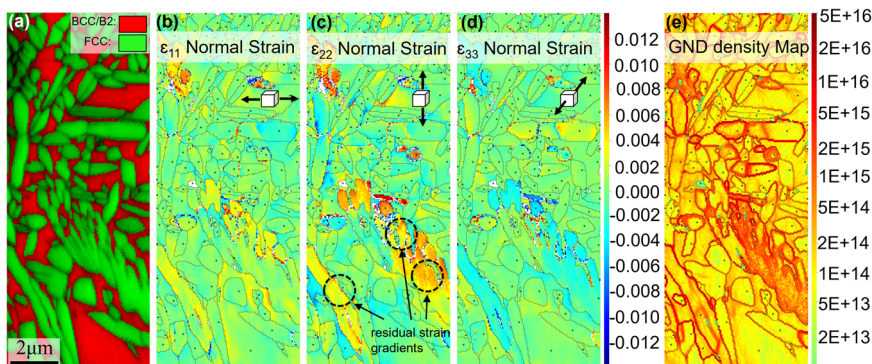


**Table 2 | Printing parameters for L-PBF and L-DED of AlCrFe<sub>2</sub>Ni<sub>2</sub> HEAs**

Processing condition	L-PBF $V = 375$ mm/s	L-DED $V = 3.3$ mm/s	L-DED $V = 4.7$ mm/s	L-DED $V = 6.2$ mm/s
Laser spot diameter (mm)	0.1	0.4	0.4	0.4
Laser power (W)	150	230	230	230
Scan speed (mm/s)	375	3.3	4.7	6.2
Hatch spacing (mm)	0.08	0.3	0.3	0.4
Layer thickness (mm)	0.04	0.25	0.25	0.25
Powder feed rate (g/min)	–	1.89	3.07	4.32

transformation pathway during AM. Using AlCrFe<sub>2</sub>Ni<sub>2</sub> as a prototype system, we observe significant phase and microstructure evolution under different printing conditions during L-PBF and L-DED. Through systematic microstructural characterization, thermal modeling, thermodynamic and kinetic consideration of phase evolution, and site-specific residual stress/strain analysis, we rationalize the fundamental mechanism of crack mitigation in additively manufactured AlCrFe<sub>2</sub>Ni<sub>2</sub> HEAs. The primary conclusions of our study are summarized as follows:

- (1) In L-PBF samples with high cooling rates ( $10^4$ – $10^6$  K/s), polycrystalline solidification results in a single-phase BCC/B2 microstructure, leading to low ductility and high susceptibility to solid-state cracking. In L-DED samples with much lower cooling rates ( $10^2$ – $10^4$  K/s), a multi-phase microstructure comprising BCC/B2 and FCC phases exhibits significantly enhanced ductility and resistance to solid-state cracking.
- (2) In L-DED samples with much slower cooling rates, the thermal cycling effect induces solid-state phase transformation in the HAZ, promoting the precipitation of the secondary FCC phase from the BCC/B2 phase. This solid-state transformation is kinetically facilitated by elemental diffusion at lower cooling rates, which allows for the tuning of the FCC phase fraction by varying the cooling rate during printing, providing an opportunity to tailor the properties of the as-printed material.
- (3) The occurrence of the secondary FCC phase in L-DED samples can accommodate thermal residual stresses through substantial plastic deformation, a feature which helps relieve thermal stresses within the BCC/B2 phase and prevent nucleation and propagation of solid-state cracks during the printing process. In contrast, L-PBF samples exhibit severe cracking due to the presence of a brittle BCC/B2 phase and the high residual stresses/strains occurring mainly at grain boundaries.

The proposed strategy of varying the thermal history to engineer the phase transformation pathway provides a versatile toolbox to mitigate residual stresses and suppress cracking in multi-component metal alloys produced by AM. Through phase transformation pathway engineering during AM, one can also achieve controlled microstructures and mechanical properties for various target applications.

## Methods

### Material fabrication

Gas-atomized powders of AlCrFe<sub>2</sub>Ni<sub>2</sub> with sizes of 15–53  $\mu\text{m}$  and 53–106  $\mu\text{m}$  were selected for L-PBF and L-DED, respectively. Plate-shaped L-PBF samples of 25 mm  $\times$  8 mm  $\times$  4 mm were printed by an EOS M290 machine (EOS, Germany) with a bi-directional scan strategy and 90° rotations in scan pattern between neighboring layers. The printing substrate was a low-carbon steel plate and was heated to 100 °C during printing. In this work, the laser beam power was set to 150 W and the scan rate was set to 375 mm/s for L-PBF after process optimization by a series of control experiments to minimize the porosity. Through this method a sample with density of  $\sim 7.210$  g/cm<sup>3</sup> was achieved (relative density:  $\sim 99.5\%$ ). The volumetric energy density (VED) of the L-PBF sample is calculated as 125 W/mm<sup>3</sup>. The L-DED plate-shaped samples with similar dimensions as those of the L-PBF samples were printed using a laser power of 230 W and three different scan speeds ( $V$ ) of 3.3 mm/s, 4.7 mm/s, and 6.2 mm/s by an Optomec LENS (laser engineered net shaping) 450 system. The VED of the L-DED  $V = 3.3$  mm/s,  $V = 4.7$  mm/s,  $V = 6.2$  mm/s samples is calculated as 929 W/mm<sup>3</sup>, 652 W/mm<sup>3</sup>, and 495 W/mm<sup>3</sup>, respectively. The powder feed rate during L-DED process was optimized for each scan speed to produce near-full density ( $\geq 99.5\%$ ) samples. The density of the L-DED  $V = 3.3$  mm/s,  $V = 4.7$  mm/s,  $V = 6.2$  mm/s samples was measured as, 7.239 g/cm<sup>3</sup> (relative density: 99.8%), 7.242 g/cm<sup>3</sup> (relative density: 99.9%), and 7.211 g/cm<sup>3</sup> (relative density: 99.5%) respectively. The porosity of samples was measured by helium gas pycnometry. All samples in this work were printed in a flowing argon environment to avoid oxidation by maintaining an oxygen concentration below 1000 ppm. The printing parameters for this study are presented in Table 2. Note that the scan speed during L-DED is typically 2–3 orders of magnitude slower than during L-PBF since the laser scanning during L-DED is achieved through robotic movement of the printing substrate while the laser scanning during L-PBF is steered by a galvanometer mirror.

### Mechanical testing

Dog-bone shaped tension samples were cut out of printed plates via wire electric discharge machining with gauge dimensions of 6.5 mm (length)  $\times$  2 mm (width)  $\times$  1.5 mm (thickness). A total of three dog-bone tensile specimens were prepared for each processing condition. Uniaxial tension



tests were carried out using an Instron 5969 machine and the strain rate was set at  $2 \times 10^{-4} \text{ s}^{-1}$ . A non-contact video extensometer was used to measure the strain. To understand the different crack propagation behaviors between the crack-containing L-PBF sample and the crack-free L-DED samples, we have performed additional micro-indentation scratch experiments. Specifically, micro-indentation scratches were implemented by rastering a spheroconical diamond indenter (Brale, Rockwell type C) with a tip radius,  $R = 200 \pm 10 \text{ }\mu\text{m}$  and apex angle  $\alpha = 120^\circ \pm 1^\circ$  over a 3 mm long track length at a sliding speed of 0.1 mm/s using a normal force of 50 N.

### Material characterization

The phase constitution was measured via X-ray diffraction (XRD, PANalytical X'Pert) utilizing a  $0.05^\circ$  step size using a Cu- $K_{\alpha 1}$  X-ray source. Specimens for EBSD and optical microscopy (OM) were prepared by cutting cross-sectional rectangles parallel to the build direction from the printed plates. These cross-sections were polished with SiC abrasive papers, 1  $\mu\text{m}$  diamond suspension, and 20 nm oxide polishing suspension (OPS). The average grain size, phase fraction, and local misorientation in the printed specimens were measured by EBSD (ZEISS-Sigma SEM). CC-EBSD was performed to compare the residual stresses in the L-DED and L-PBF samples, using a JEOL JMS-6700F field emission SEM stocked with an HKL Nordlys camera. High-resolution EBSD Kikuchi patterns were recorded (in a TIFF image format and in square mode) using the JEOL JMS 6500 F SEM equipped with EDAX DigiView IV camera at a 15Kv operating voltage with a 50 nm step size. A pattern collection condition of  $\sim 0.2$  frames per second and  $1 \times 1$  binning were selected. Analysis of the CC-EBSD data was conducted using the CrossCourt 4 platform. In total, 20 regions of interest (ROIs) were chosen on each diffraction pattern to perform cross correlation analysis. A “remapping” step was carried out to minimize the impact of grain rotation on the residual stress analysis<sup>60</sup>. SEM EDS provided mapping of the distribution of elements. The fracture surfaces after tensile tests were observed using a Magellan 400 XHR field emission SEM. STEM EDS was conducted on an FEI Titan 80–300 instrument.

### Thermal modeling and thermodynamic calculation of phase diagram

In the present work, we applied the finite volume method to simulate the heat transportation during thermal cycling under AM conditions. The energy conservation equation is described by:

$$\frac{\partial(\rho_f I)}{\partial t} = \nabla \cdot (k \nabla T) + q_l \quad (1)$$

where  $\rho_f$ ,  $k$ ,  $T$  are the mass density, thermal conductivity, and temperature of the material, respectively.  $I = \int_{T_r}^T C_p(T) dT + (1 - f_s) L_m$  is the specific internal energy of the material, where  $L_m$  is the material's latent heat of melting,  $T_r$  the reference temperature set at 273 K and  $C_p(T)$  the specific heat. The solid phase fraction  $f_s = (T - T_s)/(T_l - T_s)$  is defined as a linear interpolation of the solidus temperature ( $T_s$ ) and the liquidus temperature ( $T_l$ ).  $q_l$  represents the energy absorbed by the material, which is given as:

$$q_l(x, y, z) = \eta_l * \left[ \frac{1}{\delta \int_0^{+\infty} \exp(-\xi^2) d\xi} \exp\left(-\frac{z^2}{\delta^2}\right) \right] * Q(x, y) \quad (2)$$

The second and third terms on the right side of Eq. (2) describe the energy distribution along the  $z$ -direction and the  $x$ - $y$  directions (note the laser power is not included in the second term as it is included in the third term of the equation). The energy distribution inside the cross-section of the laser  $Q(x, y)$  is assumed to be a Gaussian distribution, which is given as:

$$Q(x, y) = \frac{PN}{2\pi R_b^2} \exp\left[-\frac{Nr^2}{2R_b^2}\right] \quad (3)$$

where  $r$  is the length away from the middle of the beam cross-section,  $P$  the laser power,  $N$  the concentration coefficient of the laser beam, and  $R_b$  the radius of the laser beam. In the simulation, we define the beam radius as the region surrounding the center of the beam that contains 99% of the beam energy, thus  $N$  is fitted with a value of 4.6 to account for this. The distribution of energy along the  $z$ -direction is defined based on a previous study<sup>61</sup>. The denominator in the second term of Eq. (2) serves as a normalization factor to ensure the integral of that term along the  $z$ -direction equals 1.  $\eta_l$  and  $\delta$  are the laser absorption coefficient and the characteristic penetration depth, respectively, which are calibrated to fit the dimensions of melt pools as measured by optical microscopy. In this study,  $z = 0$  is set at the upper boundary of the melt pool. The temperature at the lower boundary of the simulation domain is fixed at 380 K to mimic the temperature elevation of the substrate during the stable layer printing. At the other five boundaries, heat convection and heat radiation contributions are considered, which are defined as:

$$-k \nabla T \cdot \vec{n} = h(T - T_g) + e \delta_s (T^4 - T_g^4) \quad (4)$$

where  $h$  is the heat transfer coefficient of convection between the material and gas,  $\delta_s$  the Stefan-Boltzmann constant,  $e$  the emissivity factor, and  $T_g$  the ambient temperature.

The equilibrium solidification pathway and elemental partitioning in AlCrFe<sub>2</sub>Ni<sub>2</sub> HEA were simulated via the Thermo-Calc software (version TC2019a). The HEA thermodynamic database (v. TCHEA 2.1.1.) was used for extracting the thermodynamic parameters. The calculation provides a baseline of the equilibrium phase formation which we can compare with our experimental observations. The discrepancies in the predicted and observed phase fractions and phase compositions stem from the highly non-equilibrium kinetics involved in AM. This comparison allows us to extrapolate the effect of tuning the thermodynamic conditions of AM towards and away from equilibrium conditions and thus we can understand the role of kinetics in the overall phase transformation pathway.

### Data availability

The data that support the findings of this study are available from the corresponding author upon reasonable request.

Received: 20 November 2023; Accepted: 5 June 2024;  
Published online: 18 June 2024

### References

1. Blakey-Milner, B. et al. Metal additive manufacturing in aerospace: A review. *Mater. Des.* **209**, 110008 (2021).
2. Frazier, W. E. Metal additive manufacturing: a review. *J. Mater. Eng. Perform.* **23**, 1917–1928 (2014).
3. Kenel, C. et al. In situ investigation of phase transformations in Ti-6Al-4V under additive manufacturing conditions combining laser melting and high-speed micro-X-ray diffraction. *Sci. Rep.* **7**, 16358 (2017).
4. Lu, Y. et al. Controllable additive manufacturing of gradient bulk metallic glass composite with high strength and tensile ductility. *Acta Mater.* **206**, 116632 (2021).
5. Liu, Y. et al. Microstructure and mechanical behavior of additively manufactured CoCrFeMnNi high-entropy alloys: Laser directed energy deposition versus powder bed fusion. *Acta Mater.* **250**, 118884 (2023).
6. Wang, Y. M. et al. Additively manufactured hierarchical stainless steels with high strength and ductility. *Nat. Mater.* **17**, 63–71 (2018).
7. Kumara, C., Balachandramurthi, A. R., Goel, S., Hanning, F. & Moverare, J. Toward a better understanding of phase transformations in additive manufacturing of Alloy 718. *Mater* **13**, 100862 (2020).
8. Herzog, D., Seyda, V., Wycisk, E. & Emmelmann, C. Additive manufacturing of metals. *Acta Mater.* **117**, 371–392 (2016).

9. Chen, Y. et al. In-situ Synchrotron imaging of keyhole mode multi-layer laser powder bed fusion additive manufacturing. *Appl. Mater. Today* **20**, 100650 (2020).
10. Mooraj, S., Dong, J., Xie, K. Y. & Chen, W. Formation of printing defects and their effects on mechanical properties of additively manufactured metal alloys. *J. Appl. Phys.* **132**, 225108 (2022).
11. Wang, L., Guo, Q., Chen, L. & Yan, W. In-situ experimental and high-fidelity modeling tools to advance understanding of metal additive manufacturing. *Int. J. Mach. Tools Manuf.* **193**, 104077 (2023).
12. Wolff, S. J. et al. In situ X-ray imaging of pore formation mechanisms and dynamics in laser powder-blown directed energy deposition additive manufacturing. *Int. J. Mach. Tools Manuf.* **166**, 103743 (2021).
13. Bustillos, J., Kim, J. & Moridi, A. Exploiting lack of fusion defects for microstructural engineering in additive manufacturing. *Addit. Manuf.* **48**, 102399 (2021).
14. DebRoy, T. et al. Additive manufacturing of metallic components – Process, structure and properties. *Prog. Mater. Sci.* **92**, 112–224 (2018).
15. Wang, L., Zhang, Y., Chia, H. Y. & Yan, W. Mechanism of keyhole pore formation in metal additive manufacturing. *npj Comput Mater.* **8**, 22 (2022).
16. Cunningham, R. et al. Keyhole threshold and morphology in laser melting revealed by ultrahigh-speed x-ray imaging. *Science* **363**, 849–852 (2019).
17. Vrancken, B., Ganeriwala, R. K., Martin, A. A. & Matthews, M. J. Microcrack mitigation during laser scanning of tungsten via preheating and alloying strategies. *Addit. Manuf.* **46**, 102158 (2021).
18. Vrancken, B., Ganeriwala, R. K. & Matthews, M. J. Analysis of laser-induced microcracking in tungsten under additive manufacturing conditions: Experiment and simulation. *Acta Mater.* **194**, 464–472 (2020).
19. Fu, J., Li, H., Song, X. & Fu, M. W. Multi-scale defects in powder-based additively manufactured metals and alloys. *J. Mater. Sci. Technol.* **122**, 165–199 (2022).
20. Iveković, A., Montero-Sistiaga, M. L., Vleugels, J., Kruth, J.-P. & Vanmeensel, K. Crack mitigation in Laser Powder Bed Fusion processed Hastelloy X using a combined numerical-experimental approach. *J. Alloy. Compd.* **864**, 158803 (2021).
21. Kou, S. A criterion for cracking during solidification. *Acta Mater.* **88**, 366–374 (2015).
22. Sun, Z. et al. Thermodynamics-guided alloy and process design for additive manufacturing. *Nat. Commun.* **13**, 4361 (2022).
23. Martin, J. H. et al. 3D printing of high-strength aluminium alloys. *Nature* **549**, 365–369 (2017).
24. Chauvet, E. et al. Hot cracking mechanism affecting a non-weldable Ni-based superalloy produced by selective electron Beam Melting. *Acta Mater.* **142**, 82–94 (2018).
25. Sun, Z. et al. Reducing hot tearing by grain boundary segregation engineering in additive manufacturing: example of an Al<sub>x</sub>CoCrFeNi high-entropy alloy. *Acta Mater.* **204**, 116505 (2021).
26. Niu, P. et al. Inhibiting cracking and improving strength for additive manufactured Al<sub>x</sub>CoCrFeNi high entropy alloy via changing crystal structure from BCC-to-FCC. *Addit. Manuf.* **71**, 103584 (2023).
27. Talignani, A. et al. A review on additive manufacturing of refractory tungsten and tungsten alloys. *Addit. Manuf.* **58**, 103009 (2022).
28. Hofmann, D. C. et al. Compositionally graded metals: A new frontier of additive manufacturing. *J. Mater. Res.* **29**, 1899–1910 (2014).
29. Vogiatzief, D. et al. Laser powder bed fusion and heat treatment of an AlCrFe<sub>2</sub>Ni<sub>2</sub> high entropy alloy. *Front. Mater.* **7**, 248 (2020).
30. Li, N., Zhang, J., Xing, W., Ouyang, D. & Liu, L. 3D printing of Fe-based bulk metallic glass composites with combined high strength and fracture toughness. *Mater. Des.* **143**, 285–296 (2018).
31. George, E. P., Raabe, D. & Ritchie, R. O. High-entropy alloys. *Nat. Rev. Mater.* **4**, 515–534 (2019).
32. Yeh, J.-W. et al. Nanostructured high-entropy alloys with multiple principal elements: novel alloy design concepts and outcomes. *Adv. Eng. Mater.* **6**, 299–303 (2004).
33. Cantor, B., Chang, I. T. H., Knight, P. & Vincent, A. J. B. Microstructural development in equiatomic multicomponent alloys. *Mater. Sci. Eng. A* **375–377**, 213–218 (2004).
34. Kottke, J. et al. Tracer diffusion in the Ni–CoCrFeMn system: Transition from a dilute solid solution to a high entropy alloy. *Scr. Mater.* **159**, 94–98 (2019).
35. Otto, F. et al. Decomposition of the single-phase high-entropy alloy CrMnFeCoNi after prolonged anneals at intermediate temperatures. *Acta Mater.* **112**, 40–52 (2016).
36. Kube, S. A. & Schroers, J. Metastability in high entropy alloys. *Scr. Mater.* **186**, 392–400 (2020).
37. Han, T. et al. Refined microstructure and enhanced mechanical properties of AlCrFe<sub>2</sub>Ni<sub>2</sub> medium entropy alloy produced via laser remelting. *J. Mater. Sci. Technol.* **99**, 18–27 (2022).
38. Han, T. et al. Effect of annealing on microstructure and mechanical properties of AlCrFe<sub>2</sub>Ni<sub>2</sub> medium entropy alloy fabricated by laser powder bed fusion additive manufacturing. *Mater. Sci. Eng.: A* **839**, 142868 (2022).
39. Dong, Y., Gao, X., Lu, Y., Wang, T. & Li, T. A multi-component AlCrFe<sub>2</sub>Ni<sub>2</sub> alloy with excellent mechanical properties. *Mater. Lett.* **169**, 62–64 (2016).
40. Molina, V. R., Weisheit, A., Gein, S., Hecht, U. & Vogiatzief, D. Laser metal deposition of ultra-fine duplex AlCrFe<sub>2</sub>Ni<sub>2</sub>-based high-entropy alloy. *Front. Mater.* **7**, 275 (2020).
41. Guo, L. et al. Effects of elemental segregation and scanning strategy on the mechanical properties and hot cracking of a selective laser melted FeCoCrNiMn-(N,Si) high entropy alloy. *J. Alloy. Compd.* **865**, 158892 (2021).
42. Sun, Z. et al. Revealing hot tearing mechanism for an additively manufactured high-entropy alloy via selective laser melting. *Scr. Materialia* **168**, 129–133 (2019).
43. Tang, Y. T. et al. Alloys-by-design: Application to new superalloys for additive manufacturing. *Acta Mater.* **202**, 417–436 (2021).
44. Jung, H. Y. et al. Bulk nanostructured AlCoCrFeMnNi chemically complex alloy synthesized by laser-powder bed fusion. *Addit. Manuf.* **35**, 101337 (2020).
45. Porter, D. A. *Phase Transformations in Metals and Alloys*. (CRC Press, Boca Raton, FL, 2009).
46. Guo, Y. et al. Effects of electromagnetic pulse treatment on spinodal decomposed microstructure, mechanical and corrosion properties of AlCoCrFeNi high entropy alloy. *J. Alloy. Compd.* **889**, 161676 (2021).
47. Ren, J. et al. Strong yet ductile nanolamellar high-entropy alloys by additive manufacturing. *Nature* **608**, 62–68 (2022).
48. Xin, T. et al. Ultrahigh specific strength in a magnesium alloy strengthened by spinodal decomposition. *Sci. Adv.* **7**, eabf3039 (2021).
49. Fan, W. et al. Partially melted powder in laser based directed energy deposition: Formation mechanism and its influence on microstructure. *Int. J. Mach. Tools Manuf.* **192**, 104072 (2023).
50. Dai, G. et al. Grain refinement and columnar-to-equiaxed transition of Ti6Al4V during additive manufacturing via different laser oscillations. *Int. J. Mach. Tools Manuf.* **189**, 104031 (2023).
51. Zhang, D. et al. Additive manufacturing of ultrafine-grained high-strength titanium alloys. *Nature* **576**, 91–95 (2019).
52. Harrison, P. L. & Farrar, R. A. Application of continuous cooling transformation diagrams for welding of steels. *Int. Mater. Rev.* **34**, 35–51 (1989).
53. Panda, J. P. et al. Studies on kinetics of BCC to FCC phase transformation in AlCoCrFeNi equiatomic high entropy alloy. *Met. Mater. Trans. A* **52**, 1679–1688 (2021).
54. Markov, I. V. *Crystal growth for beginners: fundamentals of nucleation, crystal growth and epitaxy*. (World Scientific, New Jersey, 2016).
55. Charkhchian, J. et al. Spinodal Decomposition of B<sub>2</sub>-phase and Formation of Cr-Rich Nano-precipitates in AlCoCrFeNi<sub>2.1</sub> Eutectic High-Entropy Alloy. *Adv. Eng. Mater.* **25**, 2300164 (2023).



56. Bai, K. et al. Unexpected spinodal decomposition in as-cast eutectic high entropy alloy Al<sub>30</sub>Co<sub>10</sub>Cr<sub>30</sub>Fe<sub>15</sub>Ni<sub>15</sub>. *Mater. Des.* **236**, 112508 (2023).
  57. Vilalta-Clemente, A. et al. Cross-correlation based high resolution electron backscatter diffraction and electron channelling contrast imaging for strain mapping and dislocation distributions in InAlN thin films. *Acta Mater.* **125**, 125–135 (2017).
  58. Guan, S. et al. Additive manufacturing of fine-grained and dislocation-populated CrMnFeCoNi high entropy alloy by laser engineered net shaping. *Mater. Sci. Eng. A* **761**, 138056 (2019).
  59. Park, J. M. et al. Nano-scale heterogeneity-driven metastability engineering in ferrous medium-entropy alloy induced by additive manufacturing. *Acta Mater.* **221**, 117426 (2021).
  60. Britton, T. B. & Wilkinson, A. J. High resolution electron backscatter diffraction measurements of elastic strain variations in the presence of larger lattice rotations. *Ultramicroscopy* **114**, 82–95 (2012).
  61. Yan, W. Multi-scale modeling of electron beam melting of functionally graded materials. *Acta Mater.* **115**, 403–412 (2016).
  62. Fan, Q. et al. Ultrasonic induces grain refinement in gas tungsten arc cladding AlCoCrFeNi high-entropy alloy coatings. *Mater. Sci. Eng. A* **821**, 141607 (2021).
  63. Wen, Z. et al. Computation of stability, elasticity and thermodynamics in equiatomic AlCrFeNi medium-entropy alloys. *J. Mater. Sci.* **54**, 2566–2576 (2019).
  64. Sui, Y. et al. Microstructures and electrothermal properties of AlxCrFeNi multi-component alloys. *Vacuum* **144**, 80–85 (2017).
- performed CALPHAD modeling. Y.Z. and W.Y. performed thermal modeling. R.N. and N.A performed micro-indentation scratch tests. S.M., X.D., Y.Z., W.Y., Z.S. and Wen C. drafted the initial manuscript. Wen C. conceived, designed, and led the project. All co-authors contributed to the data analysis, discussion, and manuscript editing.

### Competing interests

The authors declare no competing interests.

### Additional information

**Supplementary information** The online version contains supplementary material available at <https://doi.org/10.1038/s43246-024-00542-z>.

**Correspondence** and requests for materials should be addressed to Zhongji Sun or Wen Chen.

**Peer review information** *Communications Materials* thanks Yong Yang and the other, anonymous, reviewer(s) for their contribution to the peer review of this work. Primary Handling Editor: John Plummer.

**Reprints and permissions information** is available at <http://www.nature.com/reprints>

**Publisher's note** Springer Nature remains neutral with regard to jurisdictional claims in published maps and institutional affiliations.

**Open Access** This article is licensed under a Creative Commons Attribution 4.0 International License, which permits use, sharing, adaptation, distribution and reproduction in any medium or format, as long as you give appropriate credit to the original author(s) and the source, provide a link to the Creative Commons licence, and indicate if changes were made. The images or other third party material in this article are included in the article's Creative Commons licence, unless indicated otherwise in a credit line to the material. If material is not included in the article's Creative Commons licence and your intended use is not permitted by statutory regulation or exceeds the permitted use, you will need to obtain permission directly from the copyright holder. To view a copy of this licence, visit <http://creativecommons.org/licenses/by/4.0/>.

© The Author(s) 2024

### Acknowledgements

W.C. at UMass Amherst acknowledges support from the US National Science Foundation (DMR-2004429 and DMR-2238204). Z.S. acknowledges support from the Career Development Fund (Grant reference No.: C222812017) and Young Individual Research Grant (Grant reference No.: M22K3c0096), A\*STAR, Singapore. W.Y. acknowledges the support by the Ministry of Education, Singapore, under its Academic Research Fund Tier 2 (MOE-T2EP50221-0013). N.A. and R.N. acknowledge the support by the Laboratory-Directed Research and Development (LDRD) program at Ames National Laboratory.

### Author contributions

S.M. developed the additive manufacturing process, fabricated the samples, and performed mechanical characterization. S.M., S.Z. and J.R. conducted optical microscopy and SEM experiments. X.D., D.R. and Z.S. performed EBSD characterization and data analysis. S.G., C.L. and Wei C.